



# Highly active and stable Pt electrocatalysts promoted by antimony-doped SnO<sub>2</sub> supports for oxygen reduction reactions



Min Yin<sup>a,b</sup>, Junyuan Xu<sup>a,c</sup>, Qingfeng Li<sup>a,\*</sup>, Jens Oluf Jensen<sup>a</sup>, Yunjie Huang<sup>a</sup>,  
Lars N. Cleemann<sup>a</sup>, Niels J. Bjerrum<sup>a</sup>, Wei Xing<sup>b,\*\*</sup>

<sup>a</sup> Department of Energy Conversion and Storage, Kemitorvet 207, Technical University of Denmark, DK-2800 Lyngby, Denmark

<sup>b</sup> Laboratory of Advanced Power Sources, Changchun Institute of Applied Chemistry, Chinese Academy of Sciences, Changchun 130022, PR China

<sup>c</sup> Department of Physical Chemistry, University of Science and Technology Beijing, 30 College Road, Beijing 100083, PR China

## ARTICLE INFO

### Article history:

Received 22 March 2013

Received in revised form 24 June 2013

Accepted 1 July 2013

Available online 12 July 2013

### Keywords:

Platinum

Antimony doped tin oxides

Support

Oxygen reduction reactions

Fuel cells

## ABSTRACT

Alternative composite supports for platinum catalysts were synthesized from antimony doped tin dioxide (ATO) nanoparticles. In the range of the antimony content from 0 to 11 mol%, the highest electrical conductivity of 1.1 S cm<sup>-1</sup> at 130 °C was obtained for the 5 mol% Sb ATO, from which composite supports composed of oxides and carbon and supported platinum catalysts were prepared. Using the pure oxide support, the Pt/ATO catalyst displayed superior specific activity and stability for the oxygen reduction reactions (ORRs). Low surface area of ATO caused poor dispersion of Pt particles compared to composite supports, which limited the mass activity of the supported catalysts. When the ATO composites were used as supports, the Pt/C-ATO catalysts showed significantly enhanced catalytic activity and durability for the ORR, attributable to the high ECSA and modified electronic structure of Pt by the ATO phase in the catalyst support.

© 2013 Elsevier B.V. All rights reserved.

## 1. Introduction

Proton exchange membrane fuel cells (PEMFCs) are emerging as a potential technology for the highly efficient and clean energy conversion [1,2]. Remarkable progress has been made in the past two decades. However, challenges remain concerning lifetime, reliability and cost, which are hindering the commercialization of the technology [3]. One of the most critical issues is the lifetime [4,5]. Degradation of the currently used carbon-supported Pt-based catalysts, especially on cathodes for the oxygen reduction reaction (ORR) [6], is well identified as a major failure mode of PEMFCs [7,8]. The proposed mechanisms that contribute to the cathode catalyst degradation include carbon support corrosion, catalyst particle sintering, and catalyst dissolution.

Carbon is the typical catalyst support material due to its high specific surface area for the dispersion of metal nanoparticles, a porous structure for transferring reactants and products, and good electrical conductivity required for electrochemical reactions [9,10]. This material is, however, susceptible to corrosive fuel cell conditions such as high cathode potentials, elevated temperature and low pH in combination with oxygen and water vapor.

Under these conditions, the carbon corrosion is thermodynamically favorable. Under idle, load-cycling or startup/shutdown modes of operation, which are a prerequisite for automobile applications, the cathode will experience potentials as high as 1.5 V, causing severe carbon corrosion [11,12]. In addition, the presence of the Pt catalyst accelerates the rate of the carbon corrosion [13,14]. The carbon corrosion, in turn, prevents electrical contact and triggers the agglomeration and sintering of Pt nanoparticles, resulting in decrease in the electrochemical surface area (ECSA) under long-term operation [15].

Other catalyst supports such as metal oxides as an alternative to carbon have received much attention recently, aiming at simultaneous enhancement of the catalytic activity and durability [16,17]. Several conductive metal oxides including TiO<sub>2</sub>, Nb<sub>2</sub>O<sub>5</sub>, SnO<sub>2</sub> and others have been investigated as catalyst supports with significantly improved stability [18–22]. High specific surface area is desirable for the oxides in order to improve the metal dispersion and increase the active site density, which is however a challenge for such oxides due to the difficulties in achieving morphological stability and sufficiently high electrical conductivity [23]. This problem can be more severe when a porous and highly disordered crystalline structure is demanded at the same time [24].

As an effective way to improve the electronic conductivity and maintain the structural functionalities, composite supports of the oxides and carbon materials by loading metal oxides onto carbon supports or coating carbon nanotubes with metal oxides have been

\* Corresponding author. Tel.: +45 45 25 23 18.

\*\* Corresponding author. Tel.: +86 434 85262223.

E-mail addresses: [qfli@dtu.dk](mailto:qfli@dtu.dk) (Q. Li), [xingwei@ciac.jl.cn](mailto:xingwei@ciac.jl.cn) (W. Xing).

proposed [25,26]. In the present study, antimony doped  $\text{SnO}_2$  (ATO) nanoparticles were first synthesized and optimized with respect to the antimony doping content and the resultant electronic conductivity. The high specific area ATO has been recently proposed to be used as support for Pt– $\text{IrO}_2$  catalysts in unitized regenerative fuel cells [27]. The ATO was screened in terms of the conductivity as well as morphology, from which composite supports with carbon blacks were prepared. Platinum particles were then loaded as catalysts for the ORR. It was found that the electronic structure of Pt was modified by the presence of the ATO phase in the catalyst supports, which was found to significantly enhance the electrochemical activity and catalyst durability toward the ORR.

## 2. Experimental

### 2.1. Catalysts preparation

ATO support nanoparticles were first synthesized as previously described [28]. In brief,  $\text{SbCl}_3$  and  $\text{SnCl}_4$  in a certain molar ratio were dissolved in distilled water containing citric acid. Ammonia water (10 wt%, Aldrich) was then added to precipitate the mixture hydroxides, which were subsequently collected by filtration. The precipitate was then dispersed in water at 70 °C and the pH was adjusted to 2 by adding oxalic acid (30 wt%, Aldrich). Polyethyleneglycol (Aldrich) was further added as a dispersion agent and the suspension was dried at 80 °C in a vacuum oven for 12 h. The resulting powders were finally calcinated at 600 °C for 1 h to obtain ATO powders. To prepare carbon-ATO composite supports, the ATO and carbon black (XVC-72R) were dispersed by sonication in de-ionized water and stirring for 24 h to obtain well-blended support materials with variable C to ATO weight ratios of 2:1, 1:1, and 1:2.

Platinum nanocatalysts supported on the carbon black (Pt/C), the ATO (Pt/ATO) and the carbon-ATO composite (Pt/C-ATO) were then prepared by a modified polyol method. Dihydrogen hexachloroplatinic acid was first dissolved in ethylene glycol. The pH of the solution was adjusted to above 10 by adding 1.0 M NaOH. After the solution was heated under refluxing to 160 °C for 3 h, the catalyst support (C, ATO or C-ATO) was added and the pH value was slowly brought down to 2 by dropwise addition of an aqueous solution of 0.1 M HCl. The suspension was then heated to 90 °C and kept for another 3 h to deposit Pt colloids onto the support. The whole preparation process was conducted under flowing nitrogen. Electrocatalysts were obtained after cooling to room temperature, washing and drying. The Pt loading was 20 wt% for all electrocatalysts.

### 2.2. Materials characterization

The crystal structure of the prepared samples was verified by X-ray diffraction (XRD) with a Rigaku-D/MAX-PC2500 X-ray diffractometer (Japan) using a  $\text{Cu K}\alpha$  ( $\lambda = 1.5405 \text{ \AA}$ ) as a radiation source operating at 40 kV and 200 mA. The specific surface area of ATO was determined by multipoint Brunauer–Emmett–Teller [11] analysis of the nitrogen adsorption isotherms recorded on a surface area analyzer (Micromeritics ASAP 2020). Transmission electron microscopy (TEM) analysis was carried out with a JEOL2010 microscope operating at 200 kV with nominal resolution. Samples were first ultrasonicated in ethanol for 1 h and then deposited on 3 mm Cu grids. X-ray photoelectron spectroscopy (XPS) analysis was taken on a Kratos XSAM-800 spectrometer with an Al  $\text{K}\alpha$  monochromatic source. The Pt 4f signals were collected and analyzed with deconvolution of the spectra using XPS Peak software. The electrical conductivity was measured by electrochemical impedance spectroscopy in a range of 1–10<sup>6</sup> Hz and ac amplitude of 10 mV [29]. Samples were pressed into pellets with a diameter

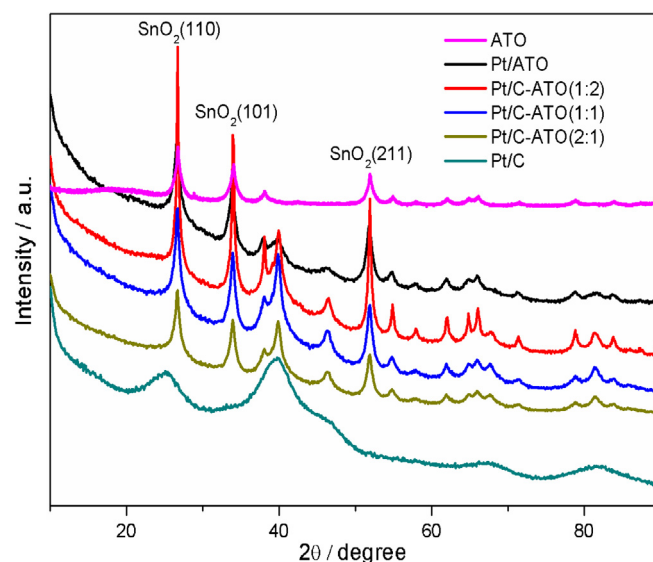


Fig. 1. XRD patterns of ATO, Pt nanoparticles supported on carbon, ATO and carbon-ATO.

of 13 mm and a thickness of about 2 mm under a pressure of  $4.9 \times 10^8 \text{ Pa}$ . A gold mesh as the current collector was placed on each side of a pellet and assembled in a cell. Measurements were performed at 25, 80 and 130 °C.

### 2.3. Electrochemical characterizations

All the electrochemical measurements were carried out with a Princeton Versastat 3 Potentiostat with a Pt coil as the counter electrode and saturated calomel electrode (SCE) as the reference electrode. The catalyst ink was prepared by ultrasonically dispersing 5.0 mg catalyst in 50  $\mu\text{L}$  Nafion and 1 mL ethanol for 30 min. The rotating-disk electrode (RDE) with a diameter of 5 mm and a geometric area of  $0.2 \text{ cm}^2$  served as an underlying substrate of the working electrode. A quantity of 4.2  $\mu\text{L}$  of the dispersion was pipetted on the top of the electrode. Finally, the electrode was obtained after the solvent volatilized. All the tests were performed at ambient temperature.

Cyclic voltammograms (CVs) recorded in  $\text{N}_2$ -saturated  $0.5 \text{ mol L}^{-1} \text{ H}_2\text{SO}_4$  solution were used to obtain the background capacitive currents and electrochemical surface area (ECSA) of the Pt catalysts. The ECSA of Pt was determined by charge integration under the hydrogen desorption peaks assuming a charge of  $210 \mu\text{C cm}^{-2}$  for a monolayer of hydrogen adsorbed on polycrystalline platinum. The electrolyte was purged with oxygen for 30 min prior to the oxygen reduction measurement. Linear sweep voltammetry (LSV) was then conducted at a scan rate of  $10 \text{ mV s}^{-1}$  and a rotation speed of 1600 rpm. The electrode rotation speed was controlled by Model 636 Ring-Disk Electrode System. The ORR kinetic current values were obtained with the Koutecky–Levich equation. The activity of each catalyst was compared at 0.6 V (vs. SCE). The stability of the catalysts was considered by the potential cycling experiments within the potential range of 0.35–0.85 V (vs. SCE) at scan rate of  $50 \text{ mV s}^{-1}$  under an oxygen atmosphere. The CVs and oxygen-reduction polarization curves were recorded before and after stability test.

## 3. Results and discussions

The synthesized ATO nanoparticles and the Pt catalysts were analyzed by XRD, as shown in Fig. 1. The diffraction peaks of ATO show a typical polycrystalline diffraction of the cassiterite  $\text{SnO}_2$ .

**Table 1**  
Conductivity of tin dioxide and antimony doped tin dioxide supports ( $\text{S cm}^{-1}$ ).

Temperature ( $^{\circ}\text{C}$ )	Antimony content (wt%) in (Sb + Sn)				
	0	3	5	8	11
25	0.0023	0.09	0.83	0.73	0.446
80	0.0027	0.102	0.99	0.86	0.683
130	0.00325	0.116	1.13	1.01	0.803

No phase ascribed to antimony oxides could be seen, indicating the possible entrance of antimony into tin oxide lattice, which was in agreement with the reported results [30].

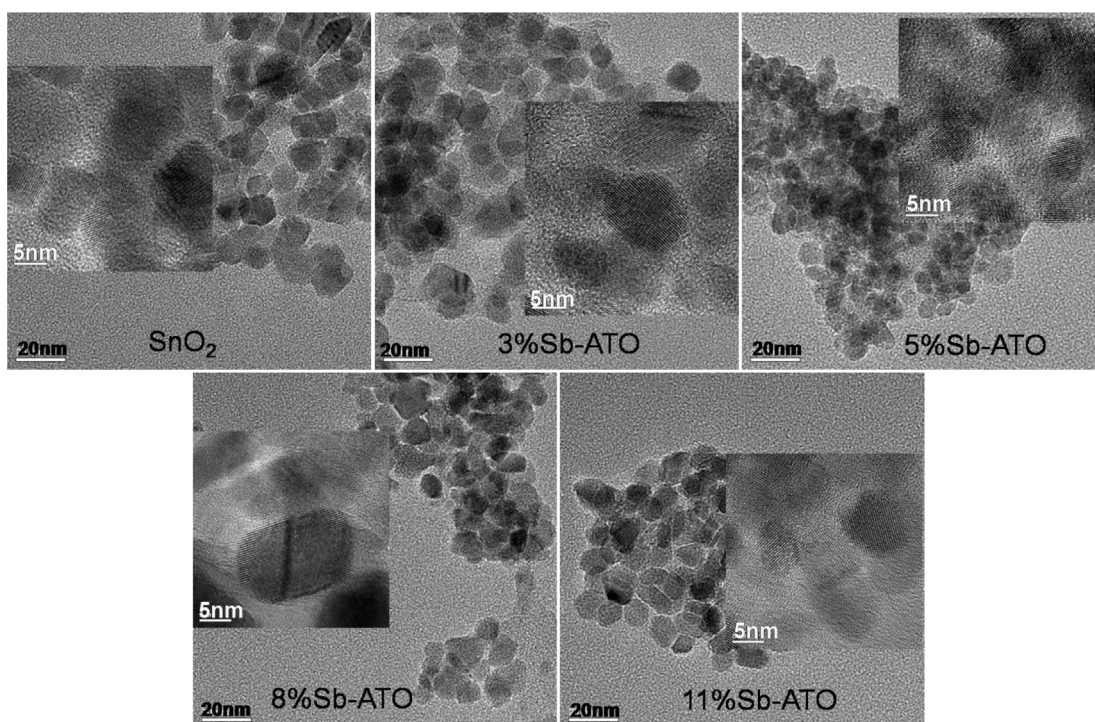
The conductivity of tin oxides and antimony doped tin oxides is listed in Table 1. While the as prepared  $\text{SnO}_2$  showed an electronic conductivity of  $0.0023 \text{ S cm}^{-1}$  at  $25^{\circ}\text{C}$ , the antimony doped  $\text{SnO}_2$  exhibited an immensely increased conductivity, in good agreement with literature [31,32]. At an atomic doping level of 5% Sb, the optimum composition, the conductivity reached as high as  $0.83 \text{ S cm}^{-1}$  at room temperature. At higher antimony contents, e.g. at an Sb molar content of 8% and 11%, the conductivity was found to level off with a slight decrease. This was explained by the possible competition between the two oxidation states of antimony,  $\text{Sb}^{5+}$  and  $\text{Sb}^{3+}$ , as proposed by Terrier [33]. At low doping levels, the  $\text{Sb}^{5+}$  ions were dominant and the substitution of  $\text{Sn}^{4+}$  by the n-type dopant  $\text{Sb}^{5+}$  would generate more oxygen vacancies and therefore led to an increase in the conductivity. When the Sb content was further increased, the  $\text{Sb}^{5+}$  dopant is gradually replaced by  $\text{Sb}^{3+}$ , compensating the oxygen vacancies, i.e., inducing the p-type doping and hence decrease in conductivity. At elevated temperatures of 80 and  $130^{\circ}\text{C}$ , a slight increase in the conductivity was observed for pure  $\text{SnO}_2$  and ATO powders. For the 5% Sb-ATO, the conductivity was found to be 0.99 and  $1.13 \text{ S cm}^{-1}$  at 80 and  $130^{\circ}\text{C}$ , respectively.

TEM images of ATO with different Sb doping contents are shown in Fig. 2. It was found that the  $\text{SnO}_2$  and all the ATO nanoparticles are uniform and spherical. The insets showed the high resolution TEM (HRTEM) of the oxides. The well-defined fringes of each sample could be found from the insets of Fig. 2, which demonstrated the

good crystallinity of the obtained oxides. The average size of  $\text{SnO}_2$  nanoparticles was found to be ca. 10.0 nm. As Sb was doped into the oxide, the average size of 3% Sb-ATO was found to be decreased into ca. 9.3 nm. At an atomic doping level of 5% Sb, the average size was further decreased to ca. 6.5 nm. As the content of Sb increased to higher levels at 8% and 11%, the average size was found to increase to 8.6–8.7 nm, still smaller than that of the undoped  $\text{SnO}_2$ . In addition, the specific surface areas of the obtained samples were also measured from the BET analysis and found to be 21, 30, 50, 35, and  $57 \text{ m}^2 \text{ g}^{-1}$  for the antimony content of 0, 3, 5, 8 and 11% in the ATO, while that of the commercial Vulcan XC-72R carbon black was measured to be  $240 \text{ m}^2 \text{ g}^{-1}$ . Based on the above conductivity, morphology and the BET results, the ATO containing 5% Sb was selected for preparation of composite supports with carbon and supported catalyst for further evaluation.

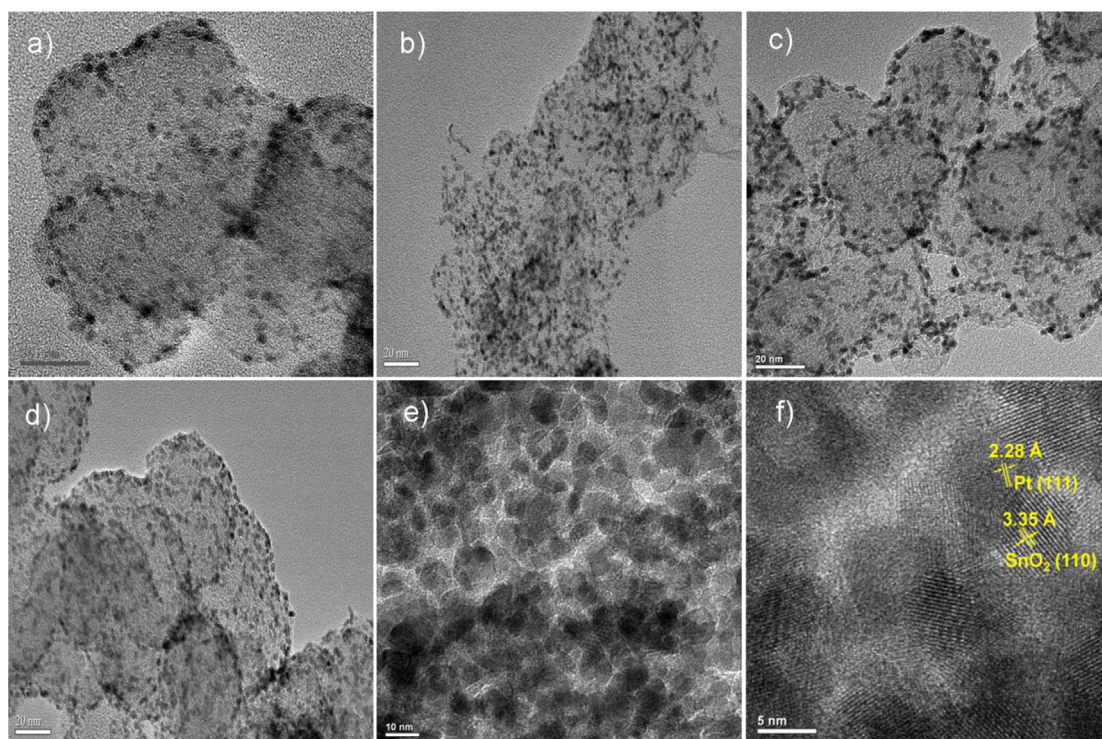
The as-prepared Pt catalysts displayed the characteristic pattern of the face-centered cubic (fcc) structure from the XRD patterns. The diffraction peaks at around  $39^{\circ}$ ,  $46^{\circ}$  and  $68^{\circ}$  were due to the diffractions at Pt (1 1 1), (2 2 0), and (2 2 0) planes, respectively. Diffraction patterns of Pt/ATO and Pt/C-ATO catalysts exhibited diffraction peaks from both Pt and ATO phases. The relative diffraction peaks of ATO were found to increase with the increased ATO-loading. The crystallite size of Pt in each catalyst could be calculated by using Scherrer's equation and found to be 4.0, 4.5, 4.8, 4.3, and 2.6 nm for Pt/ATO, Pt/C-ATO (1:2), Pt/C-ATO (1:1), Pt/C-ATO (2:1), and Pt/C catalyst, respectively, showing a strong dependence of the Pt particle size on the supports.

Fig. 3 displays the TEM images of Pt/C, Pt/ATO and Pt/C-ATO samples. For Pt/ATO catalyst, Pt particles covered most of the ATO surface and stacked on top of one another. The HRTEM image of the Pt/ATO catalyst indicated the very good crystallinity of ATO from the well-defined fringes at 3.35 Å, which corresponded to the spacing of plane  $\text{SnO}_2$  (1 1 0). The fringes with lattice spacing of 2.28 Å were indexed as (1 1 1) of the fcc Pt. The Pt nanoparticles were found to be well anchored on the ATO supports. The distribution of Pt particles became remarkable as it was loaded on carbon and C-ATO hybrid supports. As seen from Fig. 3a–d, the Pt particles



**Fig. 2.** TEM images of antimony doped tin oxides with different content of antimony in the oxide. The insets are the high resolution TEM images of each sample.





**Fig. 3.** TEM images of (a) Pt/C, (b) Pt/C-ATO (2:1), (c) Pt/C-ATO (1:1), (d) Pt/C-ATO (1:2), (e) Pt/ATO, and (f) the high resolution TEM images of Pt/ATO.

were evenly distributed on the carbon and C-ATO composite surface. Due to the large volume content and the large surface area of carbon, compared with ATO, the Pt and ATO nanoparticles were both deposited on carbon surface. It is then hard to distinguish the particle size of Pt from TEM due to the similar size of Pt and ATO, though the XRD analysis and the associated calculation revealed a steady increase in the Pt particle size when ATO and ATO composites were employed as supports instead of their counterpart of carbon blacks. It should be remarked that the variation of the platinum particle size influences both the activity and stability of the catalysts, which makes the following performance comparison of these catalysts less straightforward than being expected.

The electronic structure change of Pt from ATO modification was determined by XPS. As shown in Fig. 4, the Pt 4f signals of each sample were deconvoluted into three components assigned to metallic Pt (0), Pt (II) and Pt (IV) species. The binding energies of Pt 4f<sub>7/2</sub> along with the relative densities of Pt (0) for each catalyst are listed in Table 1. It was found that the BE of the metallic Pt was gradually shifted to the lower energy with the increased ATO content on the supports, and the lowest binding energy of Pt 4f was observed on the Pt/ATO catalyst. This result indicated the modulated interactions between Pt and supports by introduction of the ATO. The possible electron transfer from Sn to Pt was also suggested to be responsible for the observed BE shift [34,35]. On the other hand, the content of Pt (0) was found to be gradually increased from 38.8% for Pt/C to 51.4% for the Pt/ATO with increasing the ATO content on supports (see Table 2), further demonstrating the strong metal-support interactions between Pt and ATO. The higher content of Pt (0) also illuminated that the Pt in the Pt/ATO possessed higher stability due to the greater corrosion resistance of Pt (0) [36].

Fig. 5a shows the CVs of each catalyst in N<sub>2</sub>-saturated 0.5 M H<sub>2</sub>SO<sub>4</sub>. All the samples exhibited the H-adsorption/desorption peaks at −0.2 to 0.1 V and the Pt-oxide formation/reduction peak at ~0.65/0.5 V. The ECSA value of each catalyst was calculated from the hydrogen desorption peak, as shown in Fig. 5b. Even though the crystallite size of Pt in Pt/ATO from XRD was found to be slightly

smaller than that of Pt/C-ATO, the Pt particles were found to overlap each other and show the poor distribution on ATO, both effects leading to a decrease of the Pt utilization of the catalysts. In addition, the relative low electrical conductivity and the small surface area of ATO jointly resulted in the smallest ECSA (20 m<sup>2</sup> g<sup>−1</sup>) of Pt/ATO catalyst. A comparable ECSA was then obtained for Pt supported on the carbon-ATO composite, compared with that on carbon supports. Moreover, the ECSA was found to increase with a small quantity of ATO in the composite supports such as C-ATO (2:1), most likely attributable to the better interactions between Pt and ATO containing supports, as compared with the Pt/C catalyst. However, the ECSA was found to decrease as the C to ATO mass ratio reached 1:2, primarily resulted from the decreased surface area of supports as the ATO content was increased. The optimal ECSA was therefore obtained on the Pt/C-ATO (2:1) catalyst due to the appropriate balance between the surface area and the metal–support interaction.

The catalytic activity of each catalyst for ORR was evaluated in the O<sub>2</sub>-saturated 0.5 M H<sub>2</sub>SO<sub>4</sub> solution, as shown in Fig. 5c. The well-defined mass transfer and kinetic regions were observed on all the catalysts. The ORR was under mixed kinetic-diffusion control in the potential region between 0.6 V and 0.35 V, followed by a region where the diffusion limiting current was observed. A smaller diffusion limiting current observed on the Pt/ATO catalyst could be attributed to the relatively smaller surface area of ATO compared to that of carbon. The catalytic activity could be first assessed from the half-wave potential (*E*<sub>1/2</sub>). It was found that all Pt/C-ATO catalysts

**Table 2**

Quantitative data of the fits of Pt 4f<sub>7/2</sub> XPS spectra for each sample.

Catalyst	BE of Pt (0) (eV)	Values of Pt (0) in % in the total intensity
Pt/C	71.8	38.8
Pt/C-ATO (2:1)	71.75	44.1
Pt/C-ATO (1:1)	71.7	46.3
Pt/C-ATO (1:2)	71.58	49.5
Pt/ATO	71.34	51.4

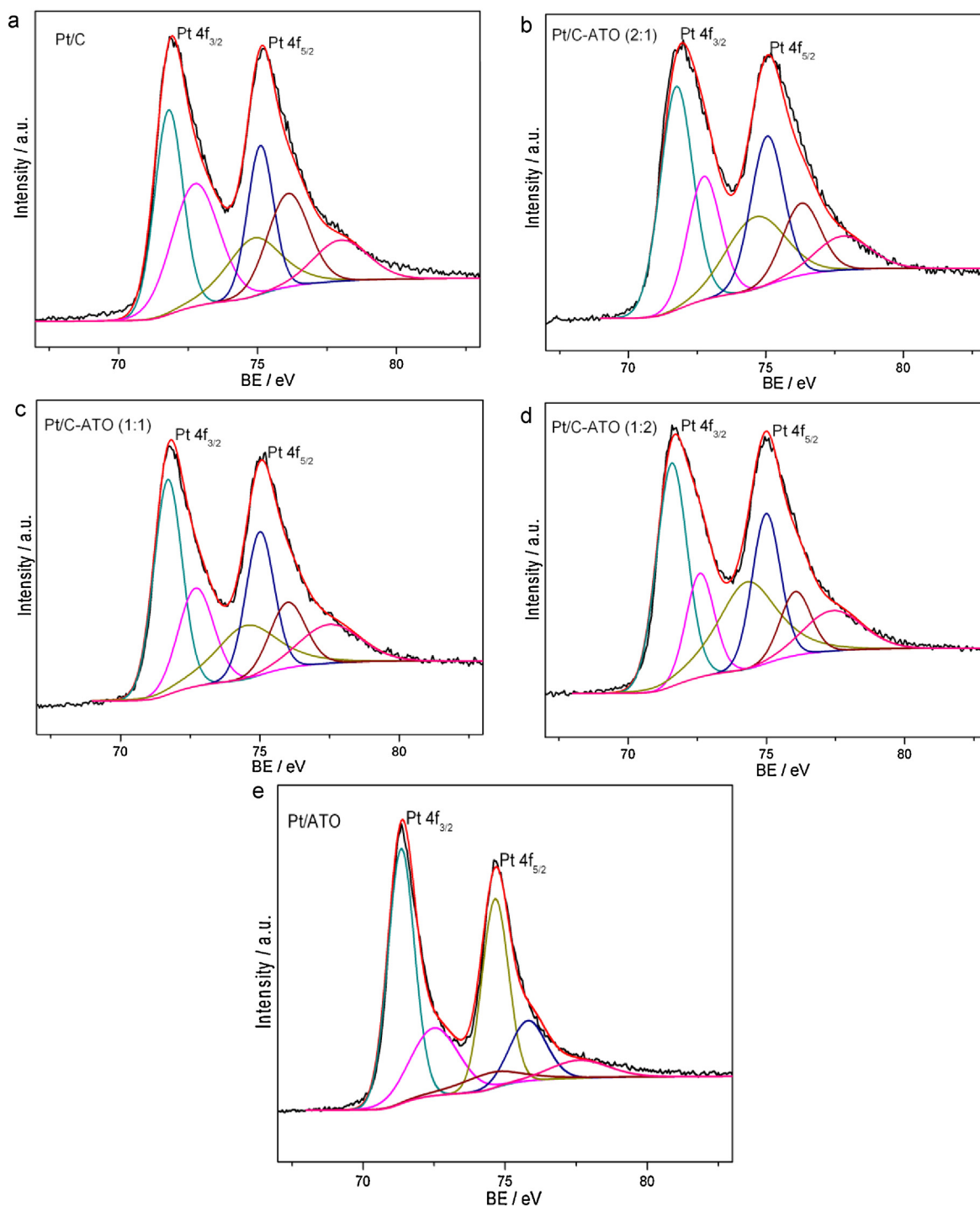
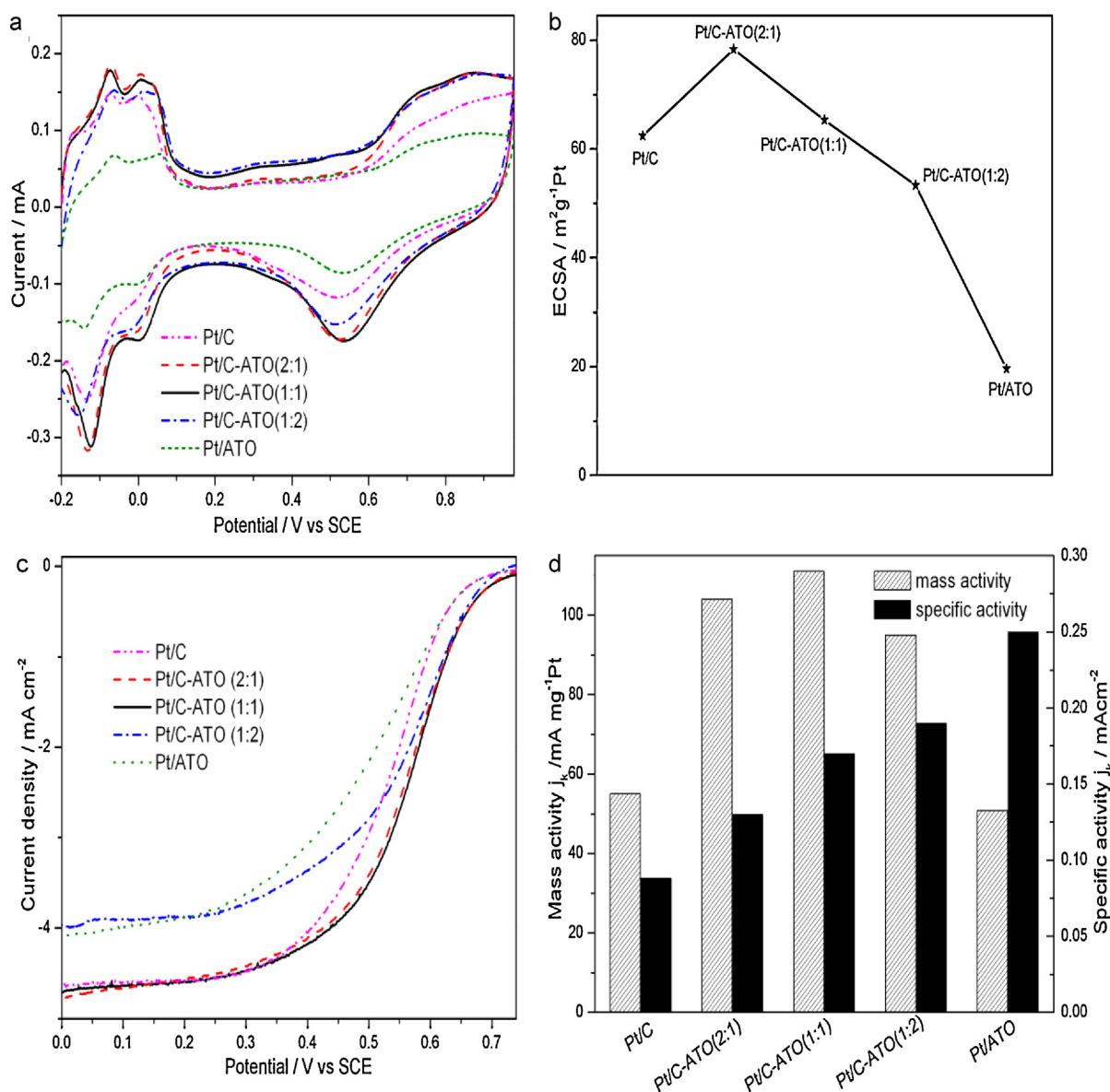


Fig. 4. XPS spectra of Pt/C, Pt/ATO, and Pt/C-ATO samples.

exhibited more positive  $E_{1/2}$  than that for the Pt/C catalyst, indicating the more efficient ORR on Pt/C-ATO catalysts than that on the Pt/C catalyst. The catalytic activity of each catalyst was then compared by kinetic currents according to the Levich–Koutecky equation [37]. The currents were normalized by the Pt mass and real Pt surface area. As shown in Fig. 5d, the specific activity of Pt was found to increase gradually with the increased ATO content and the Pt/ATO catalyst showed the best specific activity, which means that ATO greatly enhanced the intrinsic catalytic activity of Pt for the ORR.

In general, the ORR on the metal surface involves the dissociative adsorption of  $O_2$  and subsequent electroreduction and removal of the adsorbed oxygen atoms [38,39]. It was reported that the adsorption energy (AE) of oxygen could be a descriptor of the specific activity of catalysts toward ORR based on the atomic adsorption pathway. An appropriate AE value is required to balance the progress of  $O_2$  dissociation and adsorbed oxides removal for the most efficient ORR [40–42]. Pt binds oxygen a little too strongly so that the removal of the oxygen species to refresh the active site limits the overall ORR kinetics.



**Fig. 5.** (a) CVs of each catalyst in N<sub>2</sub>-saturated 0.5 M H<sub>2</sub>SO<sub>4</sub> solutions at a scan rate of 50 mV s<sup>-1</sup>, (b) calculated ECSA value of each catalyst, (c) ORR polarization curves of each catalyst in O<sub>2</sub>-saturated 0.5 M H<sub>2</sub>SO<sub>4</sub> solutions at a scan rate of 10 mV s<sup>-1</sup> and a rotation of 1600 rpm, and (d) mass and specific activity for ORR at 0.6 V vs. SCE for each sample.

In the present study, it was found that ATO could strongly modify the electronic structure of Pt, as evidenced from above XPS results. This happened to alter the AE of oxygen on Pt surface and consequently facilitate the consecutive oxygen reduction, which resulted in the observed high specific activity of ATO modified Pt catalysts. The gradual increase of the specific activity of Pt could be attributed to the gradual alternation of Pt electronic structure with the increased ATO content. However, for Pt/ATO electrocatalyst, the smaller ECSA value greatly inhibited the Pt electrocatalytic utilization on ORR, which resulted in the smaller mass catalytic activity for ORR on Pt/ATO catalysts, as compared with that on the Pt/C catalyst. The superior mass catalytic activity on ORR was obtained for Pt/C-ATO catalysts because the ECSA was greatly increased by fabricating the carbon-ATO composites as supports. The best mass activity was obtained on the Pt/C-ATO (1:1) catalyst with about 2 times as high as that on the Pt/C catalyst due to the coordinating optimization of both ECSA and specific activity.

The stability is the key challenge for PEM fuel cell technology. The electrochemical stability of each catalyst was evaluated by a potential cycling with a cycling number of up to 3000 in the O<sub>2</sub>-saturated H<sub>2</sub>SO<sub>4</sub> solution. The potential cycling causes the dissolution and precipitation of Pt into and from the electrolyte. At the same time, carbon oxidation would be accelerated during the cycling, triggering the platinum sintering. In addition, the OH species adsorbed on the catalyst could also oxidize the carbon support, forming gaseous carbon dioxide [43,44]. The eventual result would be catalyst agglomeration, causing a decrease in the ECSA of the catalyst.

Fig. 6 displays the CVs and ORR polarization curves before and after the potential cycling for 3000 cycles. For each catalyst the corresponding histograms of ECSA and ORR kinetic currents at 0.6 V (vs. SCE) are shown in Fig. 7. The stabilities of catalysts were found to increase in the order of Pt/C < Pt/C-ATO (2:1) < Pt/C-ATO (1:1) < Pt/C-ATO (1:2) < Pt/ATO. It should be noted that almost no ECSA and ORR catalytic activity degradation was observed on the



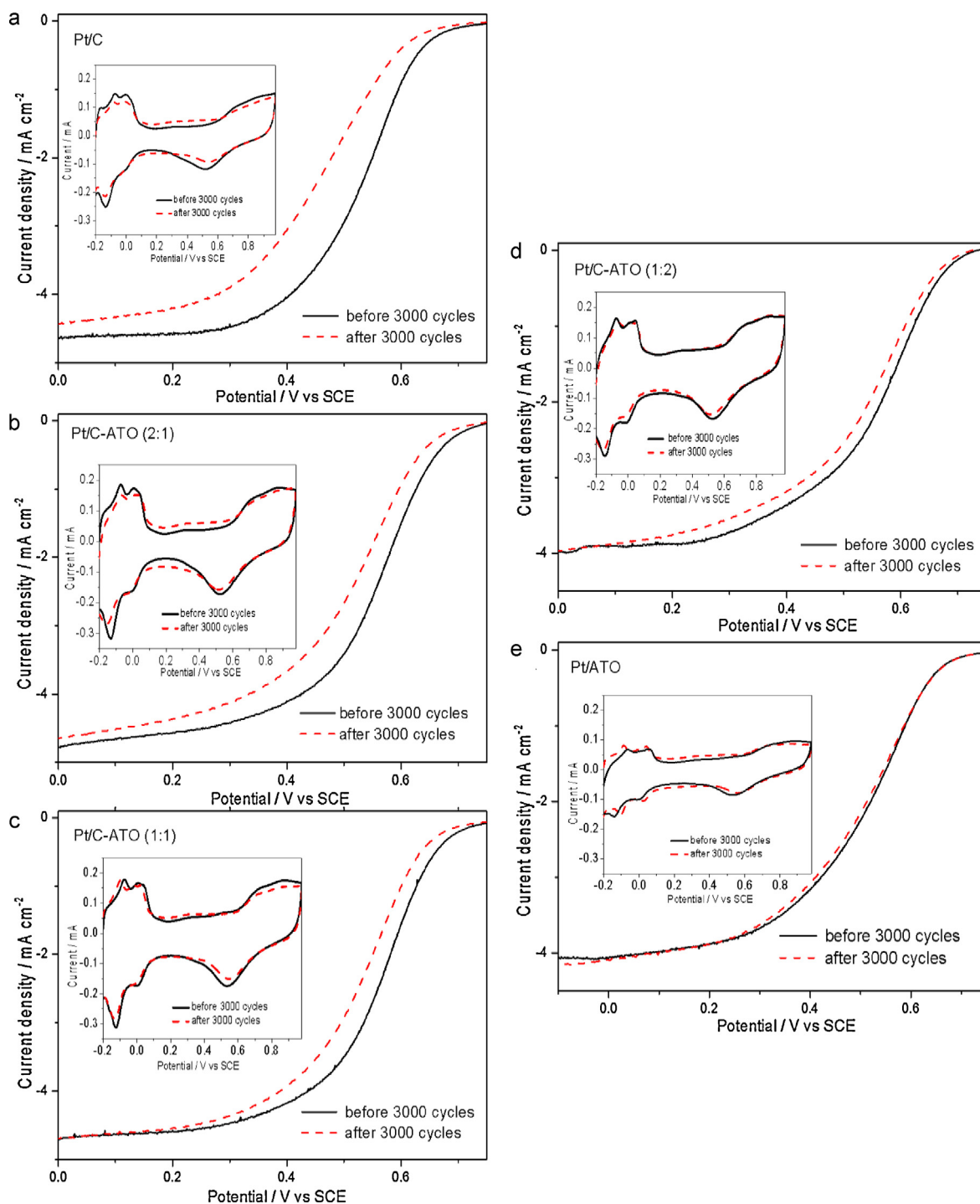


**Fig. 6.** ORR polarization curves of each catalyst in  $O_2$ -saturated 0.5 M  $H_2SO_4$  solutions at a scan rate of  $10 \text{ mV s}^{-1}$  and a rotation of 1600 rpm before and after 3000 cycles between potential of 0.35 and 0.85 V at a scan rate of  $50 \text{ mV s}^{-1}$ . The insets are the CVs of each catalyst in  $N_2$ -saturated 0.5 M  $H_2SO_4$  solutions before and after degradation tests.

Pt/ATO catalyst, while the most severe decrease of the ECSA and catalytic activity occurred on the Pt/C catalyst. It demonstrated that the substitution of carbon by ATO could greatly improve the stability of Pt catalyst. Chang prepared  $TiO_2$  grafted on carbon and carbon-supported Pt catalysts and studied catalyst deactivation at high temperatures ( $>130^\circ\text{C}$ ). They concluded that the  $TiO_2$  was able to anchor Pt particles by interacting with Pt, thereby inhibiting Pt migration and agglomeration [45]. The stability of  $Pt/Nb_xTi_{(1-x)}O_2$  was also investigated and found the 59% loss of catalytic activity after 2500 cycles under the potential range of 0–1.2 V [18].

The superior stability of Pt/ATO catalysts were also found in the reported work on methanol and ethanol electrooxidation [30]. The best stability was found on 5% Pt/ATO catalyst, which possessed the 75% of the origin catalytic activity after 100 cycles.

In the present work, the highly stable properties of ATO-doped Pt/C catalysts could be first of all due to the fact that the ATO itself has superior stability under electrochemical environments. Additionally, more metallic Pt (0) existed on the Pt/ATO catalyst than on the Pt/C catalyst. Modification of the electronic structure of Pt by the presence of the ATO phase in the catalyst supports was found

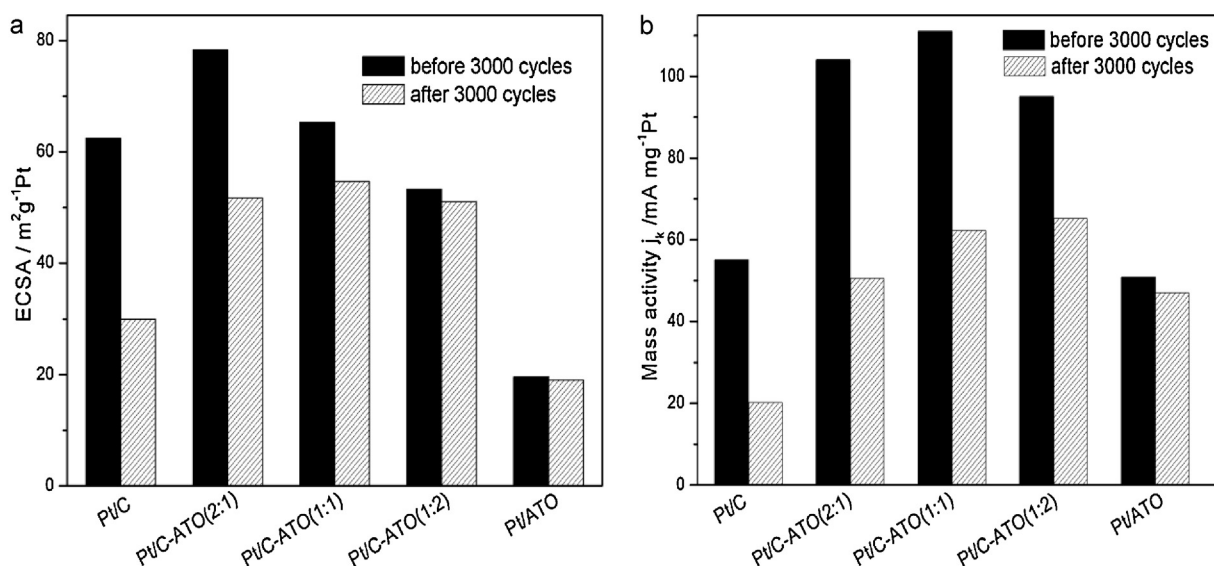


Fig. 7. Comparison of ECSA and ORR kinetic currents for each catalyst before and after degradation test in 0.5 M H<sub>2</sub>SO<sub>4</sub> solutions.

to significantly enhance the electrochemical activity and catalyst durability toward the ORR. In other words, Pt nanoparticles on the ATO support were more stable than that on the carbon support. Moreover, the particle size was also believed to affect the Pt stability under electrochemical conditions. Generally speaking, smaller particles, especially those of less than 2 nm are more unstable than bigger nanoparticles under high potentials or potential sweep conditions, which may be partially responsible for the destabilization of Pt on carbon supports, as compared with that on ATO and C-ATO supports. However, the stability of Pt nanoparticles with the similar size could be then compared on the Pt/ATO and all Pt/C-ATO catalysts. When ATO was used as a dopant to the carbon supports, the stability of Pt catalysts was found to be gradually increased with the increased ATO content, showing that the particle size most probably had less significant effect in the ATO-doped Pt/C catalysts. It indicates that the increased Pt (0) content in catalysts leads to more stable Pt nanoparticles as well as the improved corrosion resistance of the carbon support. Furthermore, for carbon-ATO supports, the fine structure adjustment of carbon-ATO composites would be promising to further benefit the activity and the stability of Pt nanocatalysts for the ORR.

#### 4. Conclusions

Antimony doped tin dioxide (ATO) nanoparticles were synthesized with the antimony content from 0 to 11 mol% with respect to tin. The highest electrical conductivity was obtained for the 5 mol% Sb in ATO, from which composite supports and supported platinum catalysts were prepared. Using the pure oxide support, the Pt/ATO catalyst displayed superior specific activity and stability for the ORR whereas the mass activity was low due to the low electrochemical surface area and low electrical conductivity of the support. When the ATO composites were used as supports, the Pt/C-ATO catalysts showed significantly enhanced catalytic activity for the ORR compared with that of the Pt/C catalyst. The specific activity of the Pt/C-ATO was found to steadily increase with the ATO content in the composite support phase. In term of mass activity, the best performance was achieved for the catalysts with composite supports of a carbon to ATO mass ratio of 1:1. The best performance is attributable to the high ECSA and modified electronic structure of Pt by the presence of the ATO phase in the catalyst supports, which was found to significantly enhance the catalyst durability.

#### Acknowledgements

This work was jointly supported by the Danish National Research Foundation, the Danish ForskEL Programme and Nature Science Foundation of China (21011130027). 973 Program (2012CB215500) and 863 Program (SS2012AA053401) are also acknowledged.

#### References

- [1] H.A. Gasteiger, N.M. Markovic, *Science* 324 (2009) 48–49.
- [2] M.Z. Jacobson, W.G. Colella, D.M. Golden, *Science* 308 (2005) 1901–1905.
- [3] R. Dillon, S. Srinivasan, A.S. Arico, V. Antonucci, *Journal of Power Sources* 127 (2004) 112–126.
- [4] J.R. Yu, T. Matsuura, Y. Yoshikawa, M.N. Islam, M. Hori, *Electrochemical and Solid State Letters* 8 (2005) A156–A158.
- [5] S.D. Knights, K.M. Colbow, J. St-Pierre, D.P. Wilkinson, *Journal of Power Sources* 127 (2004) 127–134.
- [6] D.M. Acosta, M.D.M. Acosta, L.A. Godinez, L.A. Contreras, S.M.D. Torres, J.L. Garcia, L.G. Arriaga, *Journal of Power Sources* 196 (2011) 9270–9275.
- [7] J. Xie, D.L. Wood, D.M. Wayne, T.A. Zawodzinski, P. Atanassov, R.L. Borup, *Journal of the Electrochemical Society* 152 (2005) A104–A113.
- [8] E. Antolini, *Journal of Materials Science* 38 (2003) 2995–3005.
- [9] E. Antolini, *Applied Catalysis B: Environmental* 88 (2009) 1–24.
- [10] K.Y. Chan, J. Ding, J.W. Ren, S.A. Cheng, K.Y. Tsang, *Journal of Materials Chemistry* 14 (2004) 505–516.
- [11] K. Kinoshita, J.A.S. Bett, *Carbon* 11 (1973) 403–411.
- [12] S.I. Pyun, E.J. Lee, T.Y. Kim, S.J. Lee, Y.G. Ryu, C.S. Kim, *Carbon* 32 (1994) 155–159.
- [13] Z. Siroma, K. Ishii, K. Yasuda, Y. Miyazaki, M. Inaba, A. Tasaka, *Electrochemistry Communications* 7 (2005) 1153–1156.
- [14] L. Li, Y. Xing, *Journal of the Electrochemical Society* 153 (2006) A1823–A1828.
- [15] Y.Y. Shao, G.P. Yin, Y.Z. Gao, *Journal of Power Sources* 171 (2007) 558–566.
- [16] A. Bauer, L. Chevallier, R. Hui, S. Cavaliere, J. Zhang, D. Jones, J. Roziere, *Electrochimica Acta* 77 (2012) 1–7.
- [17] Y. Fu, Z.D. Wei, S.G. Chen, L. Li, Y.C. Feng, Y.Q. Wang, X.L. Ma, M.J. Liao, P.K. Shen, S.P. Jiang, *Journal of Power Sources* 189 (2009) 982–987.
- [18] S.Y. Huang, P. Ganesan, B.N. Popov, *Applied Catalysis B: Environmental* 96 (2010) 224–231.
- [19] S. Yin, S. Mu, H. Lv, N. Cheng, M. Pan, Z. Fu, *Applied Catalysis B: Environmental* 93 (2010) 233–240.
- [20] A. Ignaszak, C. Song, W. Zhu, Y.J. Wang, J. Zhang, A. Bauer, R. Baker, V. Neburchilov, S. Ye, S. Campbell, *Electrochimica Acta* 75 (2012) 220–228.
- [21] S.L. Gojkovic, B.M. Babic, V.R. Radmilovic, N.V. Krstajic, *Journal of Electroanalytical Chemistry* 639 (2010) 161–166.
- [22] H.V.T. Thanh, C.J. Pan, J. Rick, W.N. Su, B.J. Hwang, *Journal of the American Chemical Society* 133 (2011) 11716–11724.
- [23] G. Buehler, D. Thoenmann, C. Feldmann, *Advanced Materials* 19 (2007) 2224.
- [24] D.F. Rohlfing, T. Brezesinski, B. Smarsly, J. Rathousky, *Superlattices and Microstructures* 44 (2008) 686–692.
- [25] Q. Lv, M. Yin, X. Zhao, C. Li, C. Liu, W. Xing, *Journal of Power Sources* 218 (2012) 93–99.
- [26] S. Shannnigarn, A. Gedanken, *Small* 3 (2007) 1189–1193.



- [27] J.C. Cruz, S. Rivas, D. Beltran, Y. Meas, R. Ornelas, G.O. Monreal, L.O. Frade, J.L. Garcia, L.G. Arriaga, *International Journal of Hydrogen Energy* 37 (2012) 13522–13528.
- [28] J.Y. Xu, Q.F. Li, M.K. Hansen, E. Christensen, A.L.T. Garcia, G.Y. Liu, X.D. Wang, N.J. Bjerrum, *International Journal of Hydrogen Energy* 37 (2012) 18629–18640.
- [29] Y. Huang, Q. Li, A.H. Jensen, M. Yin, J.O. Jensen, E. Christensen, C. Pan, N.J. Bjerrum, W. Xing, *Journal of Materials Chemistry* 22 (2012) 22452–22458.
- [30] K.S. Lee, I.S. Park, Y.H. Cho, D.S. Jung, N. Jung, H.Y. Park, Y.E. Sung, *Journal of Catalysis* 258 (2008) 143–152.
- [31] V. Muller, M. Rasp, G. Stefanic, J. Ba, S. Guenther, J. Rathousky, M. Niederberger, D.F. Rohlfling, *Chemistry of Materials* 21 (2009) 5229–5236.
- [32] T. Nutz, U. zum Felde, M. Haase, *Journal of Chemical Physics* 110 (1999) 12142–12150.
- [33] C. Terrier, J.P. Chatelon, R. Berjoan, J.A. Roger, *Thin Solid Films* 263 (1995) 37–41.
- [34] A.K. Shukla, A.S. Arico, K.M. El-Khatib, H. Kim, P.L. Antonucci, V. Antonucci, *Applied Surface Science* 137 (1999) 20–29.
- [35] K. Ke, K. Waki, *Journal of the Electrochemical Society* 154 (2007) A207–A212.
- [36] Z. Jiang, Z. Wang, Y. Chu, D. Gu, G. Yin, *Energy and Environmental Science* 4 (2011) 728–735.
- [37] H.Y. Jung, S. Park, B.N. Popov, *Journal of Power Sources* 191 (2009) 357–361.
- [38] J. Zhang, M.B. Vukmirovic, Y. Xu, M. Mavrikakis, R.R. Adzic, *Angewandte Chemie-International Edition* 44 (2005) 2132–2135.
- [39] V. Stamenkovic, B.S. Mun, K.J.J. Mayrhofer, P.N. Ross, N. Markovic, J.G. Jan Rossmeisl, J.K. Nørskov, *Angewandte Chemie-International Edition* 45 (2006) 2897–2901.
- [40] Y.G. Suo, L. Zhuang, J. Lu, *Angewandte Chemie-International Edition* 46 (2007) 2862–2864.
- [41] J. Zhang, M.B. Vukmirovic, Y. Xu, M. Mavrikakis, R.R. Adzic, *Journal of the American Chemical Society* 127 (2005) 12480–12481.
- [42] K. Gong, D. Su, R.R. Adzic, *Journal of the American Chemical Society* 132 (2010) 14364–14366.
- [43] S.Y. Ahn, S.J. Shin, H.Y. Ha, S.A. Hong, Y.C. Lee, T.W. Lim, I.H. Oh, *Journal of Power Sources* 106 (2002) 295–303.
- [44] J.G. Liu, Z.H. Zhou, X.X. Zhao, Q. Xin, G.Q. Sun, B.L. Yi, *Physical Chemistry Chemical Physics* 6 (2004) 134–137.
- [45] C.C. Shih, J.R. Chang, *Journal of Catalysis* 240 (2006) 137–150.